Development of a homography-based global DIC approach for high-angular resolution in the SEM

Clément Ernould[a,b], Benoît Beausir[a,b,*], Jean-Jacques Fundenberger[a,b], Vincent Taupin[a,b], and Emmanuel Bouzy[a,b]

[a]Université de Lorraine, CNRS, LEM3, Metz, France
[b]Laboratory of Excellence on Design of Alloy Metals for low-mAss Structures (DAMAS), University of Lorraine, Metz, France
[*]Corresponding author: e-mail address: benoit.beausir@univ-lorraine.fr

Contents

1. Introduction

1.1 Context and content of the chapter

As detailed in Chapter "Measuring elastic strains and orientation gradients by scanning electron microscopy: Conventional and emerging methods" by

Advances in Imaging and Electron Physics
ISSN 1076-5670
https://doi.org/10.1016/bs.aiep.2022.07.002

Ernould et al., the present work was conducted as part of the first author's PhD thesis at the University of Lorraine from 2017 to 2020 (Ernould, 2020; Ernould, Beausir, Fundenberger, Taupin, & Bouzy, 2020a, 2020b, 2021). It deals with the development of a high-angular resolution method for the measurement of lattice rotations and elastic strains in the scanning electron microscope. This kind of technique is known as the HR-EBSD or, more recently, the HR-TKD technique, depending on whether it is applied to electron backscatter diffraction (EBSD) patterns or transmission Kikuchi diffraction (TKD) patterns. In the following, "HR-EBSD/TKD" will be used when no distinction is needed regarding the SEM-based configuration used.

Working principle of high-angular resolution technique in the SEM is to determine the elastic deformation gradient tensor $\boldsymbol{F}^e$ between two points of the crystal from the observation of its effects on the scintillator, i.e., from the displacement field between two Kikuchi patterns, one being the "reference" pattern and the other the "target" one. The displacement field is measured with a subpixel resolution by means of digital image correlation techniques. Precise knowledge of the projection geometry as well as its variation between the two points of the crystal are required to interpret displacements in terms of lattice rotations and elastic strains. The HR-EBSD/TKD technique is insensitive to hydrostatic dilatation so the components of the deviatoric deformation gradient tensor $\hat{\boldsymbol{F}}^e$ are determined. A traction-free surface assumption (Hardin et al., 2015; Wilkinson, Meaden, & Dingley, 2006b) lifts the ambiguity.

The way the displacement field is evaluated is central to developments of the method over the years. The original method proposed by Wilkinson et al. (2006a, 2006b) is based on local translation measurements, by means of Fourier-transform based cross-correlation (FT-CC), between typically 20 to 200 small square subsets taken across the reference and target patterns. The components of $\hat{\boldsymbol{F}}^e$ are then computed by solving an overdetermined system of equations (Villert, Maurice, Wyon, & Fortunier, 2009; Wilkinson et al., 2006b). The method has been continuously improved since 2006. Since translation outliers strongly affect the solution (Britton et al., 2010), weighted iterative solving was proposed (Britton & Wilkinson, 2011). The hypothesis of a pure translation between subsets becoming unsuitable in the presence of rotations of few degrees, remapping techniques (Britton & Wilkinson, 2012; Maurice, Driver, & Fortunier, 2012; Zhu, Kaufmann, & Vecchio, 2020) pre-align a pattern with respect to the other to ensure an accurate shift measurement.

Despites several improvements, the implementation of the "local" approach suffers from gray area in the literature, and its performances are subject to controversy or contradiction as detailed in Chapter "Measuring elastic strains and orientation gradients by scanning electron microscopy: Conventional and emerging methods" by Ernould et al. More generally, guidelines in the choice of parameters (size, number, and arrangement of subsets) would also deserve some clarification. That is why the bibliographic review was extended to image registration techniques for surface displacements and deformations measurement during the first author's thesis (Ernould, 2020). Initial goal was to contribute to the development of the local method. One possibility considered was to authorize relative deformation of the subsets, according to affine transform (a square transform into a parallelogram). Such kind of transformation is largely used in the field of experimental mechanics. The idea was to draw inspiration from digital image correlation techniques typically applied to speckles patterns painted on macroscopic specimens, but also to follow general recommendations.

Actually, this has resulted in the development of a novel HR-EBSD/TKD approach (Ernould, 2020; Ernould et al., 2020a, 2021). It is a "global" approach, i.e., based on a single and large region of interest, in opposition to the original "local" approach. Relative deformation of the subset is allowed and described by a linear homography, which is a geometric transformation commonly used in computer vision to model projective transformations.

This chapter explicit the reasoning leading to the emergence of this global approach. It all starts with general notions concerning image registration, which consists in determining the spatial geometric or light intensity transformation to be applied to a target image in order to make it correspond to the reference image. The registration problem is characterized by the following four criteria (Brown, 1992), the choice for each of which will be discussed:

i. Some primitives, which correspond to the information extracted from the images and used for their registration (features, contours, pixel intensity, etc.).
ii. A type of transformation, which defines the space of solutions to be explored.
iii. A similarity criterion, which quantifies the similarity between the images.
iv. An optimization strategy, which determines the optimal transformation between the two images, i.e., the one leading to the highest similarity.

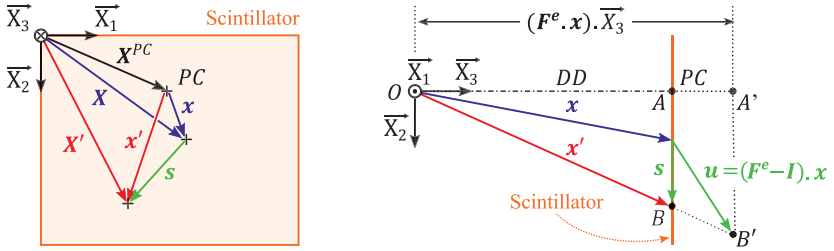

(A) Notations of points in the scintillator (B) Transformation for a fixed projection geometry

Fig. 1 Scintillator frame and points definition.

1.2 Reminder of notations and equations

Let $\left(\overrightarrow{X_1}, \overrightarrow{X_2}, \overrightarrow{X_3}\right)$ be the scintillator's frame, whose axes $\overrightarrow{X_1}$ and $\overrightarrow{X_2}$ are aligned with the scintillator's edges as shown in Fig. 1A. $\overrightarrow{X_2}$ is downwards to be consistent with the usual matrix representation of images. For the sake of clarity, points belonging to the scintillator are denoted in two ways:

- Uppercase letters, $\boldsymbol{X}=[X_1 \;\; X_2]^T$, mean that absolute (or pixel) coordinates are considered. The origin is the upper left corner of the scintillator.
- Lowercase letters, $\boldsymbol{x} = [x_1 \;\; x_2]^T$, mean that relative coordinates with respect to pattern center (PC) are considered. The latter admits $\boldsymbol{X}^{PC} = \left[X_1^{PC} X_2^{PC}\right]^T$ as absolute coordinates, i.e., $x_i = X_i - X_i^{PC}$ $(i=1, 2)$.

Let $\mathfrak{R} = \mathrm{O}\left(\overrightarrow{X_1}, \overrightarrow{X_2}, \overrightarrow{X_3}\right)$ be a coordinate system, where O is the source point of the diffraction signal, located at a distance DD away from the scintillator (Fig. 1B). A point $\boldsymbol{x} = [x_1 \;\; x_2 \;\; DD]^T$ belonging to the reference pattern is displaced by

$$\boldsymbol{u} = (\boldsymbol{F}^e - \boldsymbol{I}).\boldsymbol{x} \tag{1}$$

under the effect of the elastic deformation gradient tensor $\boldsymbol{F}^e$. This transformation induced a shift $\boldsymbol{s} = \boldsymbol{x}' - \boldsymbol{x}$ between the reference and the target patterns, where

$$\boldsymbol{x}' = \frac{DD}{(\boldsymbol{F}^e.\boldsymbol{x}).\overrightarrow{X_3}}(\boldsymbol{F}^e.\boldsymbol{x}). \tag{2}$$

This relationship is stated by Thales' theorem ($OA/OA' = OB/OB'$ in Fig. 1B) and it can be expanded as follows:

$$\begin{bmatrix} x'_1 \\ x'_2 \\ DD \end{bmatrix} = \begin{bmatrix} \dfrac{DD.\left(F^e_{11}.x_1 + F^e_{12}.x_2 + F^e_{13}.DD\right)}{F^e_{31}.x_1 + F^e_{32}.x_2 + F^e_{33}.DD} \\ \dfrac{DD.\left(F^e_{21}.x_1 + \hat{F}^e_{22}.x_2 + F^e_{23}.DD\right)}{F^e_{31}.x_1 + F^e_{32}.x_2 + F^e_{33}.DD} \\ DD \end{bmatrix}. \tag{3}$$

It constitutes the basis of all the proposed HR-EBSD/TKD techniques, so it will be referred as the "HR-EBSD/TKD problem."

2. Area-based image registration

2.1 Feature-based vs area-based methods

Determination of the transformation between images is based on a set of elements called primitives. Depending on their nature, the registration methods are qualified as feature-based or area-based, or even hybrid by combining the two previous types, as detailed in the literature review by Zitová and Flusser (2003).

Feature-based methods reduce information to few distinctive objects such as edges, line intersections, closed-boundary regions, etc. Their choice and detection are crucial. Each primitive in the reference image is then matched to the corresponding primitive in the target image to deduce the transformation. Feature-based methods are to be preferred, provided that there are sufficient primitives, distributed over the entire image while being easily detectable, distinguishable and precisely locatable.

Area-based (or intensity-based) methods consider the intensities of the pixels of the images. Therefore, they are sensitive to relative intensity variations such as noise. The absence of information reduction also makes their numerical cost higher than that of feature-based methods, especially when complex deformations are measured. For accuracy issues, the regions of interest should be as large as possible as long as its allowable relative deformations ensure a faithful description of the underlying displacement field (Pan, 2018; Pan, Qian, Xie, & Asundi, 2009; Zitová & Flusser, 2003). A contrario, smaller subsets should be considered, as is the case in the local HR-EBSD/TKD technique.

2.2 Motivations for choosing an area-based method

Kikuchi patterns contains many salient structures for which automatic detection is possible. However, their distinction raises questions. Indeed, the

diffraction contrast is not very diversified in terms of shape since it is composed exclusively of Kikuchi bands. Uniqueness of a primitive is also questioned by crystal symmetry. The implementation of a fully automated feature-based method seems therefore laborious.

Conversely, area-based methods are automatic due to the absence of data reduction. Moreover, none of the main drawbacks raised by Zitová and Flusser (2003) seem critical regarding the HR-EBSD technique:

i. The local approach has already shown that even small subsets of a Kikuchi pattern contain remarkable information.
ii. The potentially high numerical cost is nowadays counterbalanced by the increase in available computing power.
iii. Sensitivity to intensity variations can be reduced by pattern filtering and by using robust similarity criteria.

As a conclusion, an area-based method is considered.

3. Parametric description of the deformations by a homography

3.1 Shape function and homogeneous coordinates

The ability to faithfully describe the displacement field at the subset scale is paramount to measurement accuracy (Pan, 2018; Pan et al., 2009; Zitová & Flusser, 2003). A shape function is a parametric model describing the possible deformations for the subset. It involves deformation parameters, which are stored in a vector $\boldsymbol{p}$ and arranged in the shape function $\boldsymbol{W}$. The latter relates a point in the undeformed reference subset $\boldsymbol{\xi}$ to its image in the deformed target subset $\boldsymbol{\xi}'$:

$$\boldsymbol{\xi}' = \boldsymbol{W}(\mathbf{p}).\boldsymbol{\xi}. \tag{4}$$

$\boldsymbol{\xi}$ and $\boldsymbol{\xi}'$ are defined with respect to an arbitrary point X_0, the subset geometry center for instance. They are either computed from the points' absolute coordinates (uppercase letters), $\boldsymbol{\xi}=\boldsymbol{X}-\boldsymbol{X_0}$ and $\boldsymbol{\xi}'=\boldsymbol{X}'-\boldsymbol{X_0}$ (Fig. 2A), or from their coordinates relative to the PC (lowercase letters), $\boldsymbol{\xi}=\boldsymbol{x}-\boldsymbol{x_0}$ et $\boldsymbol{\xi}'=\boldsymbol{x}'-\boldsymbol{x_0}$, where $\boldsymbol{x_0}=\boldsymbol{X_0}-\boldsymbol{X}^{PC}$, $\boldsymbol{x}=\boldsymbol{X}-\boldsymbol{X}^{PC}$ and $\boldsymbol{x}'=\boldsymbol{X}'-\boldsymbol{X}^{PC}$ (Fig. 2B). Both ways give the same vector (red in Fig. 2) so there is only one notation for $\boldsymbol{\xi}$ and $\boldsymbol{\xi}'$.

Homogeneous coordinates are considered in Eq. (4). They are often preferred to Euclidean coordinates in the field of computer vision since they ease computations. To better understand, let's take a simple example like pure translation in the plane. There are two deformation parameters, namely

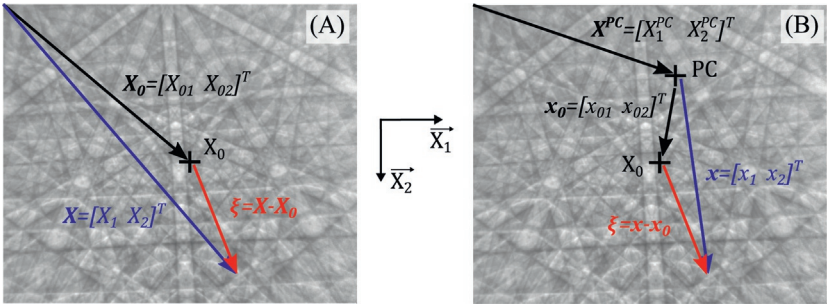

Fig. 2 Definition of the position within the reference subset ξ (A) from the points' absolute coordinates or (B) from their coordinates relative to the PC.

the shifts t_1 and t_2 along the directions $\overrightarrow{X_1}$ and $\overrightarrow{X_2}$, respectively. The deformation vector is thus: $\boldsymbol{p} = [t_1 \ \ t_2]^T$. Let $\boldsymbol{\xi} = [\xi_1 \ \ \xi_2]^T$ and $\boldsymbol{\xi}' = [\xi_1' \ \ \xi_2']^T$ be the Euclidian coordinates of a subset point in the reference and deformed configurations, respectively. It is obvious that $\xi_i' = \xi_i + t_i$ $(i = 1, 2)$, but finding a suitable shape function $\boldsymbol{W}$ to be substituted in Eq. (4) is less so. Actually, the translation is defined as follows when considering Euclidean coordinates:

$$\begin{bmatrix} \xi_1' \\ \xi_2' \end{bmatrix} = \begin{bmatrix} 1 & 0 \\ 0 & 1 \end{bmatrix} . \begin{bmatrix} \xi_1 \\ \xi_2 \end{bmatrix} + \begin{bmatrix} t_1 \\ t_2 \end{bmatrix} . \tag{5}$$

By adding an additional component as compared to Euclidean coordinates, homogeneous coordinates solve this problem:

$$\begin{bmatrix} \xi_1' \\ \xi_2' \\ 1 \end{bmatrix} = \begin{bmatrix} 1 & 0 & t_1 \\ 0 & 1 & t_2 \\ 0 & 0 & 1 \end{bmatrix} . \begin{bmatrix} \xi_1 \\ \xi_2 \\ 1 \end{bmatrix} . \tag{6}$$

A two-dimensional vector has unique Euclidean coordinates, $\boldsymbol{\xi} = [e_1 \ e_2]^T$ but it can be represented by an infinity of possible three-dimensional vectors $\boldsymbol{\xi} = [h_1 \ h_2 \ h_3]^T$ where ${h_1}^2 + {h_2}^2 + {h_3}^2 \neq 0$ when using homogeneous coordinates. Specifically, an important property of homogeneous coordinates is:

$$\forall \lambda \in \mathbb{R}^*, \ \boldsymbol{\xi} = \lambda . \boldsymbol{\xi}. \tag{7}$$

It is used to come back to Euclidean coordinates and vice versa. Indeed, when the last component in 1 in homogeneous coordinates, then other components equal those in Euclidean coordinates. In the present example, provided $h_3 \neq 0$,

it arises $h_1/h_3 = e_1$ and $h_2/h_3 = e_2$ since $\boldsymbol{\xi} = (1/h_3).\boldsymbol{\xi} = [h_1/h_3 \ h_2/h_3 \ 1]^T$ according to Eq. (7).

Note that, homogeneous coordinates prescribe finite components for any point, even those at infinity. Indeed, $h_3 = 0$ means the point is at infinity in the direction $[h_1 \ h_2]^T$.

3.2 Linear homography, a common shape function

The displacement field on the scintillator is theoretically continuous according to Eq. (2). It is thus possible to describe it with a parametric model. The latter is most often based on polynomial relationships, whose increasing order and number of parameters allows the description of more and more complex relative deformations (Sutton, Orteu, & Schreier, 2009). This is illustrated in Fig. 3 considering the most common shape functions in the literature (Brown, 1992; Sánchez, 2016; Zitová & Flusser, 2003). Quadratric (second order) shape functions are also used sometimes (Pan et al., 2009).

The local HR-EBSD technique considers a 0-order shape function, namely a translation (Fig. 3A). Affinity is largely used for surface displacement and strain measurements in experimental mechanics (Fig. 3D). Regarding Kikuchi patterns, it can account for rotations or elastic strains inducing a displacement $\boldsymbol{u}$ lying in the scintillator plane (Eq. (1) and Fig. 1B). As shown in fig. 9 in Chapter "Measuring elastic strains and orientation gradients by scanning electron microscopy: Conventional and emerging methods" by Ernould et al., only ε_{ii} ($i \in [\![1,3]\!]$), ε_{12} and w_{21} (expressed in the detector's frame) are concerned. Additional deformation parameters are necessary to describe out-of-plane effects observed with the other lattice rotation of elastic strain components.

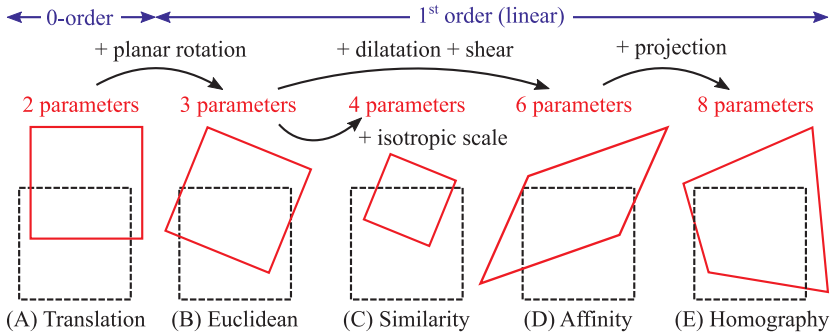

Fig. 3 Relative deformations associated with the most common shape functions in the literature.

Linear homography is a line but not angle preserving transform. It involves eight deformation parameters h_{ij} stored in the deformation vector

$$\boldsymbol{p} = [h_{11}\ h_{12}\ h_{13}\ h_{21}\ h_{22}\ h_{23}\ h_{31}\ h_{32}]^T, \tag{8}$$

and commonly arranged in the shape function as follows (Baker & Matthews, 2004; Hartley & Zisserman, 2004):

$$\boldsymbol{W}(\boldsymbol{p}) = \begin{bmatrix} 1 + h_{11} & h_{12} & h_{13} \\ h_{21} & 1 + h_{22} & h_{23} \\ h_{31} & h_{32} & 1 \end{bmatrix}. \tag{9}$$

The effect of each deformation parameters is illustrated in Fig. 4. At this point, one's notices these effects show strong similarities with the deformed configurations materialized through red quadrilaterals in fig. 9 in Chapter "Measuring elastic strains and orientation gradients by scanning electron

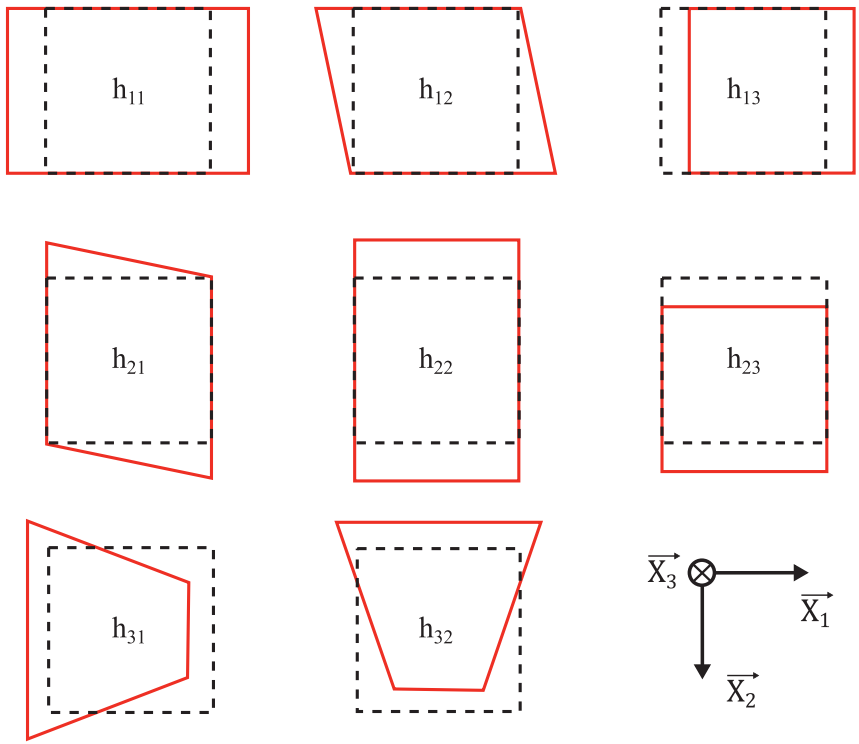

Fig. 4 Effect of each deformation parameter h_{ij} of a linear homography as parametrized in Eq. (9).

microscopy: Conventional and emerging methods" by Ernould et al. More precisely, ε_{i3} and w_{i3} looks like $\pm h_{3i}$ $(i=1, 2)$.

Injecting Eq. (9) into Eq. (4) with $\boldsymbol{\xi} = [\xi_1\ \xi_2\ 1]^T$, and then dividing by the third component, yields:

$$\begin{bmatrix} \xi'_1 \\ \xi'_2 \\ 1 \end{bmatrix} = \begin{bmatrix} \dfrac{(1+h_{11}).\xi_1 + h_{12}.\xi_2 + h_{13}}{h_{31}.\xi_1 + h_{32}.\xi_2 + 1} \\ \dfrac{h_{21}.\xi_1 + (1+h_{22}).\xi_2 + h_{23}}{h_{31}.\xi_1 + h_{32}.\xi_2 + 1} \\ 1 \end{bmatrix}. \tag{10}$$

The third components being 1, the two first components equal the Euclidean coordinates. Eq. (10) can thus be compared with the HR-EBSD/TKD problem, while keeping in mind that the method is insensitive to hydrostatic dilatation. The components of $\boldsymbol{F^e}$ are therefore substituted by those of $\hat{\boldsymbol{F}}^{\boldsymbol{e}}$ ($\hat{F}^e_{33} = 1$) in Eq. (3):

$$\begin{bmatrix} x'_1 \\ x'_2 \end{bmatrix} = \begin{bmatrix} \dfrac{DD.\left(\hat{F}^e_{11}.x_1 + \hat{F}^e_{12}.x_2 + DD\right)}{\hat{F}^e_{31}.x_1 + \hat{F}^e_{32}.x_2 + DD} \\ \dfrac{DD.\left(\hat{F}^e_{21}.x_1 + \hat{F}^e_{22}.x_2 + DD\right)}{\hat{F}^e_{31}.x_1 + \hat{F}^e_{32}.x_2 + DD} \end{bmatrix}. \tag{11}$$

The homography in Eq. (10) is analogous to the HR-EBSD/TKD problem in Eq. (11), where the third dimension is omitted since a two-dimensional transformation in the scintillator plane is considered. The question is now to know what link exists between the latter and the deformation parameters of the homography.

Note that Eq. (10) assumes $h_{31}.\xi_1 + h_{32}.\xi_2 + 1 \neq 0$, which means the homography is not degenerated, i.e., the deformed region of interested is not reduced to a straight line.

3.3 Equivalence with the HR-EBSD/TKD problem

3.3.1 *Link between* $\mathbf{h_{ij}}$ *and* $\hat{\mathbf{F}}^{\mathbf{e}}_{\mathbf{ij}}$

Since coordinates relative to the PC are considered in the HR-EBSD/TKD problem (Eq. 11), $[x_1 - x_{01}\ x_2 - x_{02}\ 1]^T$ is chosen as a possible representation of $\boldsymbol{\xi}$. By definition of the shape function, the parametrized homography in Eq. (8) yields:

$$\begin{bmatrix}\xi_1'\\ \xi_2'\\ \xi_3'\end{bmatrix}=\begin{bmatrix}(1+h_{11}).x_1+h_{12}.x_2+h_{13}-(h_{11}+1).x_{01}-h_{12}.x_{02}\\ h_{21}.x_1+(1+h_{22}).x_2+h_{23}-h_{21}.x_{01}-(1+h_{22}).x_{02}\\ h_{31}.x_1+h_{32}.x_2+1-h_{31}.x_{01}-h_{32}.x_{02}\end{bmatrix}. \tag{12}$$

Using the property in Eq. (7), the right side of Eq. (12) is multiplied by DD/β where $\beta=1-h_{31}.x_{01}-h_{32}.x_{02}$ before factoring by DD:

$$\begin{bmatrix}\xi_1'\\ \xi_2'\\ \xi_3'\end{bmatrix}=\begin{bmatrix}DD.\left(\frac{1+h_{11}}{\beta}.x_1+\frac{h_{12}}{\beta}.x_2+\frac{h_{13}-(1+h_{11}).x_{01}-h_{12}.x_{02}}{DD.\beta}.DD\right)\\ DD.\left(\frac{h_{21}}{\beta}.x_1+\frac{1+h_{22}}{\beta}.x_2+\frac{h_{23}-h_{21}.x_{01}-(1+h_{22}).x_{02}}{DD.\beta}.DD\right)\\ \frac{DD.h_{31}}{\beta}.x_1+\frac{DD.h_{32}}{\beta}.x_2+DD\end{bmatrix}. \tag{13}$$

All components are divided by the third on in Eq. (13), to get back to Euclidean coordinates. In the same way $\boldsymbol{\xi}$ is defined in Fig. 2B, $\boldsymbol{\xi'}=\boldsymbol{x'}-\boldsymbol{x_0}$, which gives:

$$\begin{bmatrix}x_1'-x_{01}\\ x_2'-x_{02}\end{bmatrix}=\begin{bmatrix}DD.\dfrac{\left(\frac{1+h_{11}}{\beta}.x_1+\frac{h_{12}}{\beta}.x_2+\frac{h_{13}-(1+h_{11}).x_{01}-h_{12}.x_{02}}{DD.\beta}.DD\right)}{\frac{DD.h_{31}}{\beta}.x_1+\frac{DD.h_{32}}{\beta}.x_2+DD}\\ DD.\dfrac{\left(\frac{h_{21}}{\beta}.x_1+\frac{1+h_{22}}{\beta}.x_2+\frac{h_{23}-h_{21}.x_{01}-(1+h_{22}).x_{02}}{DD.\beta}.DD\right)}{\frac{DD.h_{31}}{\beta}.x_1+\frac{DD.h_{32}}{\beta}.x_2+DD}\end{bmatrix} \tag{14}$$

All that remains is to isolate the x_i' coordinates. Term-by-term identification of the so-obtained expression with the HR-EBSD/TKD problem in Eq. (11) leads to the following relationships:

$$\hat{\boldsymbol{F}}^{\boldsymbol{e}}=\frac{1}{\beta_0}\begin{bmatrix}1+h_{11}+h_{31}.x_{01} & h_{12}+h_{32}.x_{01} & \frac{h_{13}-h_{11}.x_{01}-h_{12}.x_{02}+x_{01}.(\beta_0-1)}{DD}\\ h_{21}+h_{31}.x_{02} & 1+h_{22}+h_{32}.x_{02} & \frac{h_{23}-h_{21}.x_{01}-h_{22}.x_{02}+x_{02}.(\beta_0-1)}{DD}\\ DD.h_{31} & DD.h_{32} & \beta_0\end{bmatrix} \tag{15}$$

where

$$\beta_0=1-h_{31}.x_{01}-h_{32}.x_{02}.$$

A linear homography thus perfectly describes the displacement field induced on the scintillator by the elastic deformation gradient $\boldsymbol{F^e}$. Knowing the projection geometry, i.e., $(x_{01}, x_{02,\ DD})$ and the deformation parameters of the homography, the deviatoric deformation gradient $\hat{\boldsymbol{F}}^{\boldsymbol{e}}$ is analytically deduced. Conversely, the deformation parameters of the homography are derived from $\boldsymbol{F^e}$, after computing the $\hat{F}^e_{ij} = F^e_{ij}/F^e_{33}$ components

$$\begin{bmatrix} h_{11} & h_{12} & h_{13} \\ h_{21} & h_{22} & h_{23} \\ h_{31} & h_{32} & 1 \end{bmatrix} = \frac{1}{\gamma_0} \begin{bmatrix} \gamma_{11} & DD.\hat{F}^e_{12} - \hat{F}^e_{32}.x_{01} & \gamma_{13} \\ DD.\hat{F}^e_{21} - \hat{F}^e_{31}.x_{02} & \gamma_{22} & \gamma_{23} \\ \hat{F}^e_{31} & \hat{F}^e_{32} & 1 \end{bmatrix} \tag{16}$$

where

$$\begin{aligned} \gamma_0 &= DD + \hat{F}_{31}.x_{01} + \hat{F}_{32}.x_{02} \\ \gamma_{11} &= DD.\hat{F}^e_{11} - \hat{F}^e_{31}.x_{01} - \gamma_0 \\ \gamma_{22} &= DD.\hat{F}^e_{22} - \hat{F}^e_{32}.x_{02} - \gamma_0 \\ \gamma_{13} &= DD.\left[\left(\hat{F}^e_{11} - 1\right).x_{01} + \hat{F}^e_{12}.x_{02} + \hat{F}^e_{13}.DD\right] + x_{01}.(DD - \gamma_0) \\ \gamma_{23} &= DD.\left[\hat{F}^e_{21}.x_{01} + \left(\hat{F}^e_{22} - 1\right).x_{02} + \hat{F}^e_{23}.DD\right] + x_{02}.(DD - \gamma_0). \end{aligned}$$

3.3.2 Accounting for probe displacements during scan

Unless stage scanning in conducted, like in Villert et al. (2009), the projection geometry of the target pattern differs from the reference one. Let $\boldsymbol{\delta PC} = [\delta_1\ \delta_2\ \delta DD]^T$ (in Euclidean coordinates) be the probe displacement at the sample's surface, as it moves from the reference to the target point, while $(x_{01}, x_{02,\ DD})$ are the calibration parameters of the reference point.

The displacement of the PC causes a uniform translation of the target pattern with respect to the reference one, i.e., $x_i' = x_i + \delta_i$ $(i = 1,\ 2)$. Obviously, $\xi_i' = \xi_i + \delta_i$ so the shape function is

$$\boldsymbol{T} = \begin{bmatrix} 1 & 0 & \delta_1 \\ 0 & 1 & \delta_2 \\ 0 & 0 & 1 \end{bmatrix}. \tag{17}$$

A change in sample to detector distance is responsible for an isotropic scale by a factor

$$\alpha = \frac{DD - \delta DD}{DD}, \tag{18}$$

with respect to the PC, i.e., $x_i' = \alpha.x_i$ ($i=1, 2$). Be aware this formula depends on the adopted coordinates system. Here, $\vec{X}_3$ is oriented toward the screen, hence the minus sign in front of δDD. Indeed, an increase in the sample to detector distance corresponds to a negative value of δDD, but generates a magnification ($\alpha > 1$) of the Kikuchi patterns (see Chapter "Measuring elastic strains and orientation gradients by scanning electron microscopy: Conventional and emerging methods" by Ernould et al.). In practice, the scale factor is obtained more simply by dividing the sample-to-detector distance associated with the target by that associated with the reference. The shape function associated to this scale is

$$\boldsymbol{S} = \begin{bmatrix} \alpha & 0 & x_{01}.(\alpha - 1) \\ 0 & \alpha & x_{02}.(\alpha - 1) \\ 0 & 0 & 1 \end{bmatrix}. \tag{19}$$

This matrix is obtained by noticing that $\alpha.x_i = \alpha.(x_i - x_{0i}) + \alpha.x_{0i}$, hence $\xi_i' = \alpha.\xi_i + x_{01}.(\alpha - 1)$. The relative coordinates x_{0i} are defined with respect to the PC of the reference pattern, so isotropic scaling must be applied before translation. Therefore, the transformation induced by probe displacement $\boldsymbol{T.S}$.

As shown in Fig. 4, scale and translation are captured by the deformation parameters h_{11}, h_{22} and h_{13}, h_{23} of the homography, respectively. The contribution of $\boldsymbol{T.S}$ must thus be removed from the homography measured between the reference and the target patterns, before deducing $\hat{\boldsymbol{F}}^{\boldsymbol{e}}$. The corrected homography

$$\boldsymbol{W}(\hat{\boldsymbol{p}}) = (\boldsymbol{T.S})^{-1}.\boldsymbol{W}(\boldsymbol{p}) \tag{20}$$

is computed by considering the inverse transformation

$$(\boldsymbol{T.S})^{-1} = \begin{bmatrix} \frac{1}{\alpha} & 0 & -\frac{\delta_1 + x_{01}.(\alpha - 1)}{\alpha} \\ 0 & \frac{1}{\alpha} & -\frac{\delta_2 + x_{02}.(\alpha - 1)}{\alpha} \\ 0 & 0 & 1 \end{bmatrix}. \tag{21}$$

By expanding Eq. (20), the corrected deformation parameters $\hat{h}_{ij}$ are obtained as follows:

$$\begin{bmatrix} \hat{h}_{11} & \hat{h}_{12} & \hat{h}_{13} \\ \hat{h}_{21} & \hat{h}_{22} & \hat{h}_{23} \\ \hat{h}_{31} & \hat{h}_{32} & 1 \end{bmatrix} = \begin{bmatrix} \dfrac{h_{11}+1-\gamma_1.h_{31}}{\alpha}-1 & \dfrac{h_{12}-\gamma_1.h_{32}}{\alpha} & \dfrac{h_{13}-\gamma_1}{\alpha} \\ \dfrac{h_{21}-\gamma_2.h_{31}}{\alpha} & \dfrac{h_{22}+1-\gamma_2.h_{32}}{\alpha}-1 & \dfrac{h_{23}-\gamma_2}{\alpha} \\ h_{31} & h_{32} & 1 \end{bmatrix}, \tag{22}$$

where $\gamma_i = \delta_i + x_{0i}.(\alpha - 1)$ with $i = 1, 2$. Finally, $\hat{\boldsymbol{F}}^e$ is analytically deduced using in Eq. (15), in which the $\hat{h}_{ij}$ parameters are considered.

3.3.3 Consequence for the DIC measurement

A linear homography is perfectly suitable for the HR-EBSD/TKD technique. It is mathematically equivalent to the model describing the displacement field between two patterns, including effects induced by probe displacement. The deviatoric deformation gradient tensor $\hat{\boldsymbol{F}}^e$ is analytically deduced from the measure homography, of deformation vector $\boldsymbol{p}$, knowing the projection geometry of the reference and target patterns.

Consequently, only one region of interest is needed for the registration of the target pattern with respect to the reference pattern. Its size does not affect the ability of the homography to faithfully describe the displacement field. The subset must thus be chosen as large as possible to maximize measurement accuracy (Pan, 2018; Pan et al., 2009; Zitová & Flusser, 2003). Ideally it encompasses the whole pattern, but the edges of the patterns may be excluded in practice, as the signal is usually noisy there. As a conclusion, the proposed method is a homography-based global DIC approach.

4. Optimization strategy by means of an IC-GN algorithm

It is now necessary to determine, among all possible homographies, the one that ensures an optimal registration of the reference image with the target. This implies to define a similarity criterion and to have a strategy to optimize it.

4.1 Optimization by means of a steepest gradient descent method

Regarding area-based methods, an exhaustive exploration of the set of possible solutions is the only way to determine with certainty the optimal transformation between the images to be registered (Zitová & Flusser, 2003).

Such an approach is typically used for translation measurement, like the local HR-EBSD/TKD technique does. However, it is unsuitable for measuring relative deformations, as the numerical cost increases considerably (Pan et al., 2009; Zitová & Flusser, 2003).

The measurement of relative deformations with subpixel accuracy classically employs iterative gradient descent algorithms. They minimize the residuals, i.e., the sum of squared differences (SSD) of the intensities between the reference and the target subsets. This sum is the similarity criterion whose steepest direction (gradient) is calculated iteratively. For this purpose, numerical optimization methods like Newton-Raphson, Gauss-Newton or Levenberg-Marquardt are used. Since these algorithms converge towards a local minimum, they required a sufficiently accurate initial estimation of the solution so that this minimum is the global minimum of the similarity criterion. The initial guess also affects convergence speed (Pan, 2018; Pan et al., 2009).

Stochastic methods, represented in particular by genetic algorithms, offer better robustness against local optima (Pan, 2018; Pan et al., 2009). However, their use for measuring surface displacements and deformations is relatively recent. The classical steepest gradient descent methods are retained since they are widely used and their implementation benefits from a detailed literature.

4.2 Choice of the inverse-compositional Gauss-New algorithm

4.2.1 Common algorithms

The most common gradient descent algorithms are (Pan, 2018): the forward-additive Newton-Raphson (FA-NR) algorithm proposed by Bruck, McNeill, Sutton, and Peters (1989), the forward-additive Gauss-Newton (FA-GN) algorithm and the inverse-compositional Gauss-Newton (IC-GN) algorithm proposed by Baker and Matthews (2001).

All of them implement the Lucas-Kanade method (Lucas & Kanade, 1981), proposed in 1981 for measuring the optical flow, i.e., the apparent displacement field between two images. Starting with an initial guess $\boldsymbol{p_0}$, these algorithms iteratively minimize the similarity criterion with respect to the increment of deformation parameters $\boldsymbol{\Delta p}$. As their name imply, they differ in the numerical optimization scheme employed as well as the way the current estimate of the solution is updated, which will be detailed in the next section.

The Gauss-Newton algorithm is a modification of the Newton-Raphson method with simplifying assumptions decreasing its numerical cost

without altering its accuracy. The FA-NR algorithm is therefore ignored as it is 3–5 times slower than the IC-GN algorithm (Pan, Li, & Tong, 2013) while also being less robust to noise (Shao, Dai, & He, 2015). It remains to choose between the FA-GN and IC-GN algorithms. While they have similar accuracy and convergence speed, especially in the case of a linear homography (Baker & Matthews, 2004), the update procedure impacts their respective numerical cost.

4.2.2 Advantage of the inverse-compositional approach

In its original form, the Lukas-Kanade method minimizes the following similarity criterion (Lucas & Kanade, 1981; Pan, 2018):

$$C_{SSD}^{FA}(\boldsymbol{\Delta p}) = \sum_{i=1}^{N} \left[T\left(\boldsymbol{W}\left(\boldsymbol{X}^{(i)}, \ \boldsymbol{p} + \boldsymbol{\Delta p} \right) \right) - R\left(\boldsymbol{X}^{(i)} \right) \right]^2. \tag{23}$$

It is the sum of squared differences of the intensities of the undeformed reference subset R, and the target T subset deformed according to $\boldsymbol{W(p+\Delta p)}$. N is the number of points of location $\boldsymbol{X}$ forming the subset.

As shown in Fig. 5, the reference subset remains undeformed during the algorithm, whereas the target subset is deformed according to the current solution estimate $\boldsymbol{p}_n$ at the beginning of each iteration. The increment of deformation $\boldsymbol{\Delta p}$ to be applied to it in order to minimize the similarity criterion defined in Eq. (23) is calculated. The deformation parameters are then updated for the next iteration using a forward-additive scheme:

$$\boldsymbol{p} \leftarrow \boldsymbol{p} + \boldsymbol{\Delta p}. \tag{24}$$

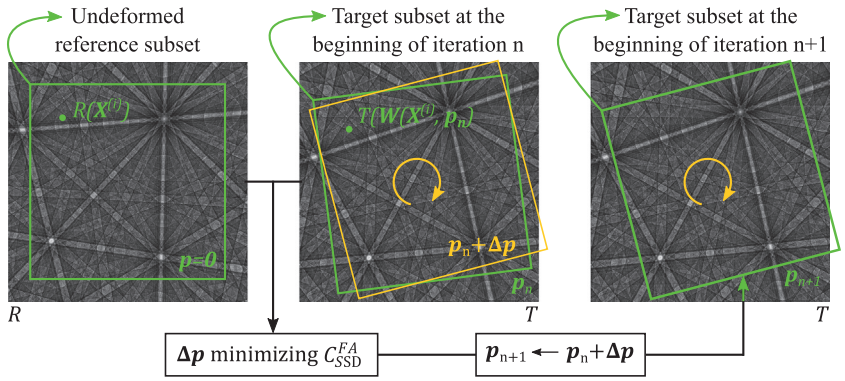

Fig. 5 Working principle of the forward-additive scheme.

In order to approximate the increment $\boldsymbol{\Delta p}$, the shape function $\boldsymbol{W}$ must be differentiable with respect to $\boldsymbol{p}$. Indeed, the Lucas-Kanade algorithm linearizes the function T by taking its Taylor series expansion to order 1 in the neighborhood of $\boldsymbol{p}_n$, $\boldsymbol{\Delta p}$ being assumed small:

$$T\left(\boldsymbol{W}\left(\boldsymbol{X}^{(i)},\ \boldsymbol{p}_n+\boldsymbol{\Delta p}\right)\right)\approx T\left(\boldsymbol{W}\left(\boldsymbol{X}^{(i)},\ \boldsymbol{p}_n\right)\right)+\left[\boldsymbol{\nabla T}\left(\boldsymbol{W}\left(\boldsymbol{X}^{(i)},\ \boldsymbol{p}_n\right)\right)\right]^T.\frac{\partial \boldsymbol{W}}{\partial \boldsymbol{p}}\left(\boldsymbol{\xi}^{(i)},\boldsymbol{p}_n\right).\boldsymbol{\Delta p} \tag{25}$$

where $\boldsymbol{\nabla T}$ are the intensity gradients of the target image and $\frac{\partial \boldsymbol{W}}{\partial \boldsymbol{p}}$ is the Jacobian of the shape function. These two quantities must be recalculated at each iteration according to the new estimate of the solution.

The inverse compositional approach is an improved version of the Lucas-Kanade method proposed by Baker and Matthews (2001). It reverses the role of the reference and the target subsets in the definition of the similarity criterion:

$$C_{SSD}^{IC}(\boldsymbol{\Delta p})=\sum_{i=1}^{N}\left[R\left(\boldsymbol{W}\left(\boldsymbol{X}^{(i)},\ \boldsymbol{\Delta p}\right)\right)-T\left(\boldsymbol{W}\left(\boldsymbol{X}^{(i)},\ \boldsymbol{p}\right)\right)\right]^2. \tag{26}$$

As shown in Fig. 6, it is now the reference subset which is allowed to deform. Like previously, the target subset is deformed according to the current solution estimate $\boldsymbol{p}_n$ at the beginning of each iteration but remains fixed during one iteration. In the inverse compositional approach, the reference subset is not deformed at the beginning of each iteration. To do so, the incremental $\boldsymbol{\Delta p}$ it must undergo is inverted and composed with the transformation already applied to the target:

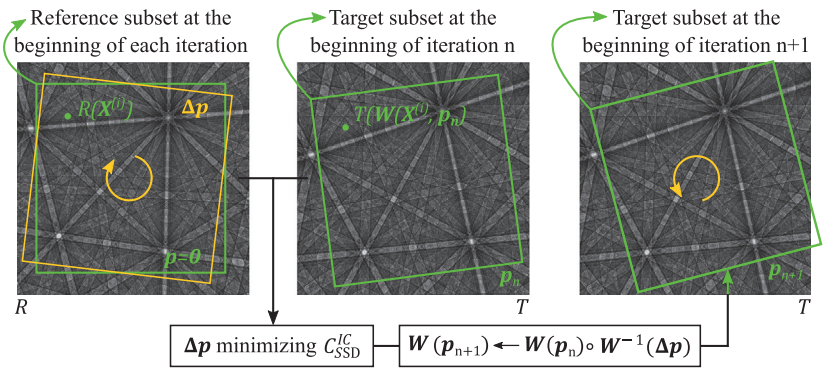

Fig. 6 Working principle of the inverse-compositional scheme.

$$\boldsymbol{W}(\boldsymbol{p}) \leftarrow \boldsymbol{W}(\boldsymbol{p}) \circ \boldsymbol{W}^{-1}(\boldsymbol{\Delta p}). \tag{27}$$

This inversion is highlighted by the orange circular arrows in Fig. 6. Instead of rotating the reference subset clockwise at the beginning of the next iteration, the target subset is updated here by undergoing a counterclockwise rotation.

The reference subset being undeformed at the beginning of each iteration, the development in Taylor series at order 1 is realized in the neighborhood of $\boldsymbol{p}=\boldsymbol{0}$:

$$R\left(\boldsymbol{W}\left(\boldsymbol{X}^{(i)},\ \boldsymbol{\Delta p}\right)\right) \approx R\left(\boldsymbol{X}^{(i)}\right) + \left[\boldsymbol{\nabla R}\left(\boldsymbol{X}^{(i)}\right)\right]^{T}.\frac{\partial \boldsymbol{W}}{\partial \boldsymbol{p}}\left(\boldsymbol{\xi}^{(i)},\ \boldsymbol{0}\right).\boldsymbol{\Delta p} \tag{28}$$

where $\boldsymbol{\nabla R}$ is the intensity gradients of the reference image and noticing that $\boldsymbol{W}(\boldsymbol{X}^{(i)},\boldsymbol{0})=\boldsymbol{X}^{(i)}$. Unlike the forward-additive approach, the intensity gradients of the reference and the Jacobian of the shape function do not depend on the current evaluation of the solution in the inverse-compositional approach. They are no longer recalculated at each iteration according to the new estimate of the solution, but pre-computed considering $\boldsymbol{p}=\boldsymbol{0}$.

In the Lucas-Kanade algorithm, the approximation in Eq. (28) is injected into the definition of the C_{SSD}^{IC} similarity criterion in Eq. (26). Since the increment $\boldsymbol{\Delta p}$ minimizes the criterion, the first derivative of C_{SSD}^{IC} with respect to $\boldsymbol{\Delta p}$ cancels, i.e.,

$$\frac{dC_{SSD}^{IC}}{d\boldsymbol{\Delta p}}(\boldsymbol{\Delta p}) = 0, \tag{29}$$

which yields:

$$\begin{aligned} &2\sum_{i=1}^{N}\left(\left[\boldsymbol{\nabla R}.\frac{\partial \boldsymbol{W}}{\partial \boldsymbol{p}}\right]^{T}.\left[R\left(\boldsymbol{X}^{(i)}\right) + \left[\boldsymbol{\nabla R}.\frac{\partial \boldsymbol{W}}{\partial \boldsymbol{p}}\right].\boldsymbol{\Delta p} - T\left(\boldsymbol{W}\left(\boldsymbol{X}^{(i)},\boldsymbol{p}\right)\right)\right]\right) \\ &= 0 \end{aligned} \tag{30}$$

where $\left[\boldsymbol{\nabla R}.\frac{\partial \boldsymbol{W}}{\partial \boldsymbol{p}}\right]$ denotes $\left[\boldsymbol{\nabla R}\left(\boldsymbol{X}^{(i)}\right)\right]^{\boldsymbol{T}}.\frac{\partial \boldsymbol{W}}{\partial \boldsymbol{p}}\left(\boldsymbol{\xi}^{(i)},\ \boldsymbol{0}\right)$ to simplify notations. Eq. (30) is rearranged by taking out $\boldsymbol{\Delta p}$ from the summation:

$$\begin{aligned} &\sum_{i=1}^{N}\left(\left[\boldsymbol{\nabla R}.\frac{\partial \boldsymbol{W}}{\partial \boldsymbol{p}}\right]^{T}.\left[\boldsymbol{\nabla R}.\frac{\partial \boldsymbol{W}}{\partial \boldsymbol{p}}\right]\right). \\ &\boldsymbol{\Delta p} = -\left[\boldsymbol{\nabla R}.\frac{\partial \boldsymbol{W}}{\partial \boldsymbol{p}}\right]\left[R\left(\boldsymbol{X}^{(i)}\right) - T\left(\boldsymbol{W}\left(\boldsymbol{X}^{(i)},\ \ \boldsymbol{p}\right)\right)\right], \end{aligned} \tag{31}$$

thus, making the Hessian matrix appear:

$$\boldsymbol{H}_{|\boldsymbol{p}=\boldsymbol{0}} = \sum_{i=1}^{N}\left(\left[\boldsymbol{\nabla R}.\frac{\partial \boldsymbol{W}}{\partial \boldsymbol{p}}\right]^{T}.\left[\boldsymbol{\nabla R}.\frac{\partial \boldsymbol{W}}{\partial \boldsymbol{p}}\right]\right). \tag{32}$$

Its calculation is the most numerically expensive step of the Gauss-Newton algorithm (Baker & Matthews, 2004). Being evaluated in $\boldsymbol{p}=\boldsymbol{0}$, it remains constant during the execution of the IC-GN algorithm, which is not the case for the FA-GN algorithm. Because of its superior numerical efficiency, the IC-GN algorithm is selected, as recommended by Pan (2018). In the framework of the HR-EBSD/TKD technique, the Hessian matrix will only need to be computed at each change of the reference image, i.e., only once per grain.

4.2.3 Zero-mean normalized correlation criterion (ZNCC)

As defined in Eq. (26), the C_{SSD}^{IC} criterion is sensitive to any variation in intensity between the reference and the target images. Its zero normalized version, denoted as C_{ZNSSD}^{IC} (ZNSSD: zero-mean normalized sum of squared differences), will be considered:

$$C_{ZNSSD}^{IC}(\boldsymbol{\Delta p}) = \sum_{i=1}^{N}\left[\frac{R\left(\boldsymbol{W}\left(\boldsymbol{X}^{(i)},\boldsymbol{\Delta p}\right)\right)-\overline{r}}{\Delta\widetilde{r}} - \frac{T\left(\boldsymbol{W}\left(\boldsymbol{X}^{(i)},\boldsymbol{p_0}\right)\right)-\overline{t}}{\Delta\widetilde{t}}\right]^{2} \tag{33}$$

$$\overline{r} = \frac{1}{N}\sum_{i=1}^{N} R\left(\boldsymbol{W}\left(\boldsymbol{X}^{(i)},\boldsymbol{\Delta p}\right)\right) \qquad \Delta\widetilde{r} = \sqrt{\sum_{i=1}^{N}\left[R\left(\boldsymbol{W}\left(\boldsymbol{X}^{(i)},\boldsymbol{\Delta p}\right)\right)-\overline{r}\right]^{2}}$$

$$\overline{t} = \frac{1}{N}\sum_{i=1}^{N} T\left(\boldsymbol{W}\left(\boldsymbol{X}^{(i)},\boldsymbol{p_0}\right)\right) \qquad \Delta\widetilde{t} = \sqrt{\sum_{i=1}^{N}\left[T\left(\boldsymbol{W}\left(\boldsymbol{X}^{(i)}\boldsymbol{p_0}\right)\right)-\overline{t}\right]^{2}}.$$

Indeed, it is insensitive to an affine variation in illumination between the two images, while providing better robustness against noise (Zitová & Flusser, 2003). Note that Kikuchi patterns will also be filtered before analysis in order to reduce noise and to subtract the continuous background resulting from inelastic electron scattering.

5. Discussion

Starting from literature reviews of digital image registration methods (Pan, 2018; Pan et al., 2009; Zitová & Flusser, 2003), an alternative

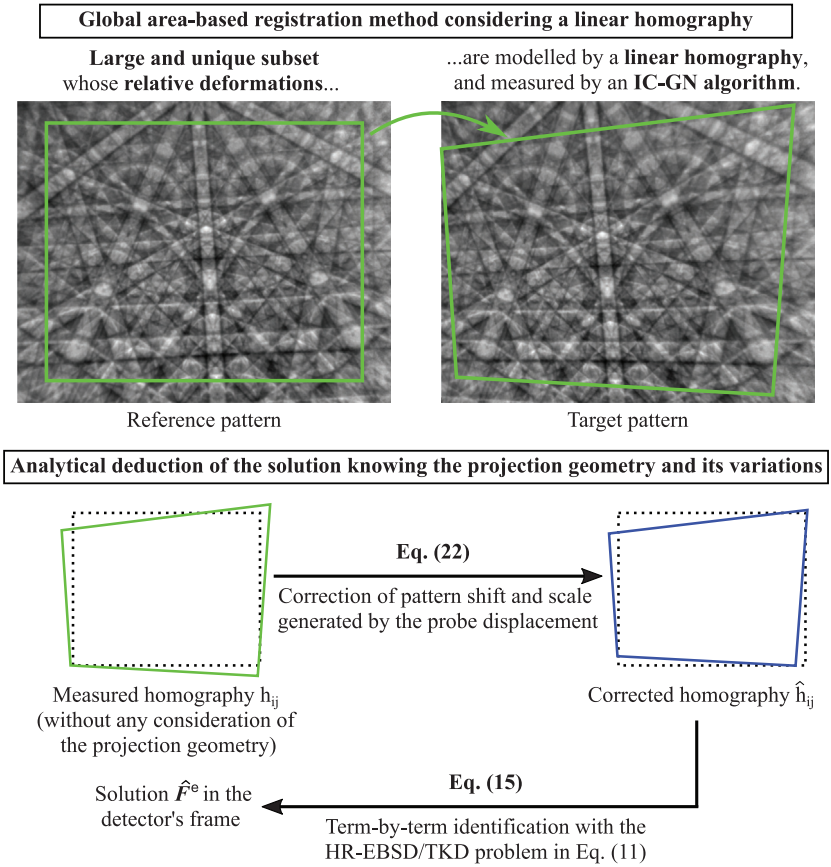

Fig. 7 Summary of the principle of the proposed global HR-EBSD/TKD technique.

HR-EBSD/TKD technique following most of their recommendations emerged. First, it is a global area-based approach. As illustrated in Fig. 7, electron diffraction patterns are analyzed as a whole, through a single large region of interest. To do so, the reference and target subsets are allowed to deform relatively according to a linear homography. This is a common shape function, often used in computer vision to model projective transformation. It involves eight deformation parameters. They are measured iteratively in the spatial domain with a subpixel resolution by means of an inverse-compositional Gauss-Newton algorithm (IC-GN). The latter minimizes the zero-mean normalized sum of squared differences in intensity of the subset, which is a similarity criterion robust to noise and insensitive to affine intensity variations.

This new approach is made possible because the displacement field described by a linear homography is mathematically equivalent to that sought in

the HR-EBSD/TKD technique at the scintillator's scale. Knowing the projection geometry, the deviatoric deformation gradient tensor $\hat{\boldsymbol{F}}^{\boldsymbol{e}}$ is analytically deduced from the measured deformation parameters h_{ij} of the homography. As summarized in Fig. 7, these are first corrected using Eq. (22) to compensate the translation and isotropic scales caused by probe displacement during the scan. Then, the solution is calculated according to Eq. (15).

Using an iterative Newton algorithm whose principle is relatively similar to the IC-GN algorithm, Hild and Roux (2012) demonstrated the superiority of global approaches over local ones in the case of a bilinear shape function. While global DIC is the strength of the proposed method, its implementation by an IC-GN algorithm nevertheless makes it sensitive to local minima. The IC-GN algorithm is indeed a local optimization scheme based on steepest gradient descent. It requires an suitable initial guess of the solution to convergence efficiently towards the global minimum of the similarity criterion. However, this algorithm is still widely used and benefits from constant improvements. It also presents a numerical efficiency superior to the other usual algorithms in its category, hence its choice.

This choice is supported by recent publications. Indeed, global HR-EBSD/TKD techniques, all based on a Gauss-Newton algorithm, were proposed in parallel to this thesis (Ruggles, Bomarito, Qiu, & Hochhalter, 2018; Shi, Roux, Latourte, & Hild, 2019; Vermeij & Hoefnagels, 2018). More precisely, Ruggles et al. (2018) also selected an IC-GN algorithm. However, stochastic methods, more robust to local optima, are likely to develop in the coming years. This statement is supported by the recent used of a differential evolution algorithm to determine the projection geometry (Tanaka & Wilkinson, 2019).

As detailed in Chapter "Measuring elastic strains and orientation gradients by scanning electron microscopy: Conventional and emerging methods" by Ernould et al., the other global HR-EBSD/TKD approaches are integrated DIC methods. They directly measure the components of the (deviatoric) deformation gradient tensor instead of the deformation parameters of the homography. Beyond its originality, the present method is at some point advantageous:

i. Image registration by the IC-GN algorithm is performed independently of any consideration of projection geometry. The locations $\boldsymbol{\xi}$ and $\boldsymbol{\xi}'$ of the points forming the reference and the target subsets, respectively, are computed from absolute coordinates in the image (Fig. 2A), as will be explained in Chapter "Implementing the homography-based global HR-EBSD/TKD approach" by Ernould et al. The uncertainty in projection geometry is not propagated at each iteration of the

IC-GN algorithm, where updating the deformed target subset is similar to the (iterative) remapping technique of the local HR-EBSD/TKD approach (Britton & Wilkinson, 2012). It only affects the analytical deduction of the solution from the measured homography, not the image registration itself.

ii. The numerical cost of an iteration of the IC-GN algorithm is reduced because the deformed coordinates are computed in a relatively straightforward way following Eq. (10), whereas Eq. (11) is used by Shi et al. (2019), and a more complex version incorporating probe displacement is considered by Vermeij & Hoefnagels (2018) and Ruggles et al. (2018). Considering a linear homography, effects of probe displacement are simply corrected using Eq. (22), which is much less computationally demanding than pre-processing all patterns, as Shi et al. (2019) did. Nonetheless, it must be recognized that a pre-processing step remains unavoidable and that it can combine several purposes. Shi et al. (2019) also corrected optical distortions for instance.

iii. Because image registration is independent from any concerns regarding the projection geometry, the solution can be recomputed quasi-instantaneously in case of change of the projection parameters.

This said, an integrated DIC approach is also justified. It eases the understanding of the algorithms, since implemented formulas correspond to the HR-EBSD/TKD model. This becomes particularly interesting in the work by Vermeij, De Graef, and Hoefnagels (2019), in which absolute elastic strains are measured from a set of diffraction patterns all associated with unrelaxed stress states. In their work, more than two patterns are considered at once. Several subsets are co-correlated, and the similarity criterion is then the sum of the similarity criteria associated to each pair of patterns to be correlated. Each pattern has its own Euler angles and projection geometry. The authors turn these into degrees of freedom of the problem, which are added to the rotations and elastic strains. Decoupling of the image registration and the different projection geometries using a set of homographies seems cumbersome.

6. Summary

- A global digital image correlation approach is proposed (Ernould et al., 2020a). Kikuchi patterns are registered as a whole, considering a unique and large region of interest, whose relative deformations are modeled by a linear homography.

- A linear homography is a first-order projective transformation. It exactly describes the theoretical displacement field in the scintillator, induced by the elastic deformation gradient tensor (Villert et al., 2009; Wilkinson et al., 2006b) as well as the effects of probe displacement.
- Eight deformation parameters h_{ij} define the linear homography (Baker & Matthews, 2004; Hartley & Zisserman, 2004). They are measured with a subpixel resolution in the spatial domain by means of an iterative inverse-compositional Gauss-Newton (IC-GN) algorithm (Baker & Matthews, 2001). Because of its numerical efficiency, this algorithm is widely used in the literature, in particular in experimental mechanics (Pan, 2018).
- The proposed method decouples image registration from calibration uncertainty. The homography between the reference and the target patterns is measured by DIC, and the projection geometry is only considered afterwards to analytically deduce the deviatoric deformation gradient tensor $\hat{\boldsymbol{F}}^{\boldsymbol{e}}$. The contribution of probe displacement effects is first removed from the measured homography using Eq. (22), and the corrected deformation parameters $\hat{h}_{ij}$ are then injected in Eq. (15) to calculate the $\hat{F}^{e}_{ij}$ components
- The similarity criterion is the zero-mean normalized sum of squared differences in the intensities of the reference and target subsets (Eq. (33)). It is insensitive to affine illumination change in the images and improves the noise robustness of the IC-GN algorithm.
- The implementation of the method is detailed in the next chapter, which also deals with the initial guess strategy. The IC-GN algorithm converges to a local optimum. It thus requires a sufficiently accurate initial guess of the solution to converge efficiently to the global optimum of the similarity criterion.

References

Baker, S., & Matthews, I. (2001). Equivalence and efficiency of image alignment algorithms. In *Vol. 1. Proceedings of the 2001 IEEE computer society conference on computer vision and pattern recognition. CVPR 2001* (pp. 1–8). https://doi.org/10.1109/CVPR.2001.990652.

Baker, S., & Matthews, I. (2004). Lucas-Kanade 20 years on: A unifying framework. *International Journal of Computer Vision*, *56*(3), 221–255. https://doi.org/10.1023/B:VISI.0000011205.11775.fd.

Britton, T. B., Maurice, C., Fortunier, R., Driver, J. H., Day, A. P., Meaden, G., et al. (2010). Factors affecting the accuracy of high resolution electron backscatter diffraction when using simulated patterns. *Ultramicroscopy*, *110*(12), 1443–1453. https://doi.org/10.1016/j.ultramic.2010.08.001.

Britton, T. B., & Wilkinson, A. J. (2011). Measurement of residual elastic strain and lattice rotations with high resolution electron backscatter diffraction. *Ultramicroscopy*, *111*(8), 1395–1404. https://doi.org/10.1016/j.ultramic.2011.05.007.

Britton, T. B., & Wilkinson, A. J. (2012). High resolution electron backscatter diffraction measurements of elastic strain variations in the presence of larger lattice rotations. *Ultramicroscopy*, *114*, 82–95. https://doi.org/10.1016/j.ultramic.2012.01.004.

Brown, L. G. (1992). A survey of image registration techniques. *ACM Computing Surveys*, *24*(4), 325–376. https://doi.org/10.1145/146370.146374.

Bruck, H. A., McNeill, S. R., Sutton, M. A., & Peters, W. H. (1989). Digital image correlation using Newton-Raphson method of partial differential correction. *Experimental Mechanics*, *29*(3), 261–267. https://doi.org/10.1007/BF02321405.

Ernould, C. (2020). *Développement et application d'une méthode à haute résolution angulaire pour la mesure des gradients d'orientation et des déformations élastiques par microscopie électronique à balayage* (These de doctorat, Université de Lorraine) http://www.theses.fr/2020LORR0225.

Ernould, C., Beausir, B., Fundenberger, J.-J., Taupin, V., & Bouzy, E. (2020a). Global DIC approach guided by a cross-correlation based initial guess for HR-EBSD and on-axis HR-TKD. *Acta Materialia*, *191*, 131–148. https://doi.org/10.1016/j.actamat.2020.03.026.

Ernould, C., Beausir, B., Fundenberger, J.-J., Taupin, V., & Bouzy, E. (2020b). Characterization at high spatial and angular resolutions of deformed nanostructures by on-axis HR-TKD. *Scripta Materialia*, *185*, 30–35. https://doi.org/10.1016/j.scriptamat.2020.04.005.

Ernould, C., Beausir, B., Fundenberger, J.-J., Taupin, V., & Bouzy, E. (2021). Integrated correction of optical distortions for global HR-EBSD techniques. *Ultramicroscopy*, *221*, 113158. https://doi.org/10.1016/j.ultramic.2020.113158.

Hardin, T. J., Ruggles, T. J., Koch, D. P., Niezgoda, S. R., Fullwood, D. T., & Homer, E. R. (2015). Analysis of traction-free assumption in high-resolution EBSD measurements. *Journal of Microscopy*, *260*(1), 73–85. https://doi.org/10.1111/jmi.12268.

Hartley, R., & Zisserman, A. (2004, March). Projective geometry and transformations of 2D. In *Multiple View Geometry in Computer Vision* (pp. 25–64). Cambridge University Press. https://doi.org/10.1017/CBO9780511811685.005.

Hild, F., & Roux, S. (2012). Comparison of local and global approaches to digital image correlation. *Experimental Mechanics*, *52*(9), 1503–1519. https://doi.org/10.1007/s11340-012-9603-7.

Lucas, B. D., & Kanade, T. (1981, April). An iterative image registration technique with an application to stereo vision. In *Proceedings of the 7th international joint conference on artificial intelligence (IJCAI '81)* (pp. 674–679).

Maurice, C., Driver, J. H., & Fortunier, R. (2012). On solving the orientation gradient dependency of high angular resolution EBSD. *Ultramicroscopy*, *113*, 171–181. https://doi.org/10.1016/j.ultramic.2011.10.013.

Pan, B. (2018). Digital image correlation for surface deformation measurement: Historical developments, recent advances and future goals. *Measurement Science and Technology*, *29*(8), 082001. https://doi.org/10.1088/1361-6501/aac55b.

Pan, B., Li, K., & Tong, W. (2013). Fast, robust and accurate digital image correlation calculation without redundant computations. *Experimental Mechanics*, *53*(7), 1277–1289. https://doi.org/10.1007/s11340-013-9717-6.

Pan, B., Qian, K., Xie, H., & Asundi, A. (2009). Two-dimensional digital image correlation for in-plane displacement and strain measurement: A review. *Measurement Science and Technology*, *20*(6), 062001. https://doi.org/10.1088/0957-0233/20/6/062001.

Ruggles, T. J., Bomarito, G. F., Qiu, R. L., & Hochhalter, J. D. (2018). New levels of high angular resolution EBSD performance via inverse compositional Gauss–Newton based digital image correlation. *Ultramicroscopy*, *195*, 85–92. https://doi.org/10.1016/j.ultramic.2018.08.020.

Sánchez, J. (2016). The inverse compositional algorithm for parametric registration. *Image Processing on Line*, *6*, 212–232. https://doi.org/10.5201/ipol.2016.153.

Shao, X., Dai, X., & He, X. (2015). Noise robustness and parallel computation of the inverse compositional Gauss–Newton algorithm in digital image correlation. *Optics and Lasers in Engineering*, *71*, 9–19. https://doi.org/10.1016/j.optlaseng.2015.03.005.

Shi, Q., Roux, S., Latourte, F., & Hild, F. (2019). Estimation of elastic strain by integrated image correlation on electron diffraction patterns. *Ultramicroscopy*, *199*, 16–33. https://doi.org/10.1016/j.ultramic.2019.02.001.

Sutton, M. A., Orteu, J. J., & Schreier, H. (2009). *Image correlation for shape, motion and deformation measurements: Basic concepts, theory and applications*. Springer US. https://doi.org/10.1007/978-0-387-78747-3.

Tanaka, T., & Wilkinson, A. J. (2019). Pattern matching analysis of electron backscatter diffraction patterns for pattern centre, crystal orientation and absolute elastic strain determination—Accuracy and precision assessment. *Ultramicroscopy*, *202*, 87–99. https://doi.org/10.1016/j.ultramic.2019.04.006.

Vermeij, T., De Graef, M., & Hoefnagels, J. (2019). Demonstrating the potential of accurate absolute cross-grain stress and orientation correlation using electron backscatter diffraction. *Scripta Materialia*, *162*, 266–271. https://doi.org/10.1016/j.scriptamat.2018.11.030.

Vermeij, T., & Hoefnagels, J. P. M. (2018). A consistent full-field integrated DIC framework for HR-EBSD. *Ultramicroscopy*, *191*, 44–50. https://doi.org/10.1016/j.ultramic.2018.05.001.

Villert, S., Maurice, C., Wyon, C., & Fortunier, R. (2009). Accuracy assessment of elastic strain measurement by EBSD. *Journal of Microscopy*, *233*(2), 290–301. https://doi.org/10.1111/j.1365-2818.2009.03120.x.

Wilkinson, A. J., Meaden, G., & Dingley, D. J. (2006a). High resolution mapping of strains and rotations using electron backscatter diffraction. *Materials Science and Technology*, *22*(11), 1271–1278. https://doi.org/10.1179/174328406X130966.

Wilkinson, A. J., Meaden, G., & Dingley, D. J. (2006b). High-resolution elastic strain measurement from electron backscatter diffraction patterns: New levels of sensitivity. *Ultramicroscopy*, *106*(4), 307–313. https://doi.org/10.1016/j.ultramic.2005.10.001.

Zhu, C., Kaufmann, K., & Vecchio, K. S. (2020). Novel remapping approach for HR-EBSD based on demons registration. *Ultramicroscopy*, *208*, 112851. https://doi.org/10.1016/j.ultramic.2019.112851.

Zitová, B., & Flusser, J. (2003). Image registration methods: A survey. *Image and Vision Computing*, *21*(11), 977–1000. https://doi.org/10.1016/S0262-8856(03)00137-9.